

## Development and evaluation of an improved quantitative 90Y bremsstrahlung SPECT method

Xing Rong, Yong Du, Michael Ljungberg, Erwann Rault, Stefaan Vandenberghe, and Eric C. Frey

Citation: *Medical Physics* **39**, 2346 (2012); doi: 10.1118/1.3700174

View online: <http://dx.doi.org/10.1118/1.3700174>

View Table of Contents: <http://scitation.aip.org/content/aapm/journal/medphys/39/5?ver=pdfcov>

Published by the [American Association of Physicists in Medicine](#)

---

**DoseWise in the OR**  
10 easy steps for effective dose management

These steps help you adhere closely to the ALARA principle (As Low As Reasonably Achievable) for X-ray dose management.

- 1. Proper system setup**  
Check to make sure equipment is properly calibrated and that the correct beam quality is used.
- 2. Use protective shielding**  
Use shields to protect patients and staff from unnecessary radiation.
- 3. Remove X-ray grid**  
When using a grid, use the correct grid-to-object distance to avoid unnecessary radiation.
- 4. Position image detector**  
Position the image detector as close to the patient as possible to reduce the amount of radiation needed to produce the image.
- 5. Maintain distance**  
Maintain a safe distance from the patient and the X-ray source to reduce radiation exposure.



Teach your staff to be DoseWise.  
Order your free poster now!

[www.philips.com/dosewiseintheor](http://www.philips.com/dosewiseintheor) **PHILIPS**

# Development and evaluation of an improved quantitative $^{90}\text{Y}$ bremsstrahlung SPECT method

Xing Rong<sup>a)</sup> and Yong Du

*Department of Radiology, Johns Hopkins University, Baltimore, Maryland 21287-0859*

Michael Ljungberg

*Department of Medical Radiation Physics, Clinical Sciences, Lund, Lund University, SE-221 85 Lund, Sweden*

Erwann Rault

*Formerly with Department of Electronics and Information Systems, MEDISIP, Ghent University-IBBT-IBiTech, De Pintelaan 185 block B, B-9000 Ghent, Belgium*

Stefaan Vandenberghe

*Department of Electronics and Information Systems, MEDISIP, Ghent University-IBBT-IBiTech, De Pintelaan 185 block B, B-9000 Ghent, Belgium*

Eric C. Frey

*Department of Radiology, Johns Hopkins University, Baltimore, Maryland 21287-0859*

(Received 10 November 2011; revised 14 March 2012; accepted for publication 14 March 2012; published 11 April 2012)

**Purpose:** Yttrium-90 ( $^{90}\text{Y}$ ) is one of the most commonly used radionuclides in targeted radionuclide therapy (TRT). Since it decays with essentially no gamma photon emissions, surrogate radionuclides (e.g.,  $^{111}\text{In}$ ) or imaging agents (e.g.,  $^{99\text{m}}\text{Tc}$  MAA) are typically used for treatment planning. It would, however, be useful to image  $^{90}\text{Y}$  directly in order to confirm that the distributions measured with these other radionuclides or agents are the same as for the  $^{90}\text{Y}$  labeled agents. As a result, there has been a great deal of interest in quantitative imaging of  $^{90}\text{Y}$  bremsstrahlung photons using single photon emission computed tomography (SPECT) imaging. The continuous and broad energy distribution of bremsstrahlung photons, however, imposes substantial challenges on accurate quantification of the activity distribution. The aim of this work was to develop and evaluate an improved quantitative  $^{90}\text{Y}$  bremsstrahlung SPECT reconstruction method appropriate for these imaging applications.

**Methods:** Accurate modeling of image degrading factors such as object attenuation and scatter and the collimator-detector response is essential to obtain quantitatively accurate images. All of the image degrading factors are energy dependent. Thus, the authors separated the modeling of the bremsstrahlung photons into multiple categories and energy ranges. To improve the accuracy, the authors used a bremsstrahlung energy spectrum previously estimated from experimental measurements and incorporated a model of the distance between  $^{90}\text{Y}$  decay location and bremsstrahlung emission location into the SIMIND code used to generate the response functions and kernels used in the model. This improved Monte Carlo bremsstrahlung simulation was validated by comparison to experimentally measured projection data of a  $^{90}\text{Y}$  line source. The authors validated the accuracy of the forward projection model for photons in the various categories and energy ranges using the validated Monte Carlo (MC) simulation method. The forward projection model was incorporated into an iterative ordered subsets-expectation maximization (OS-EM) reconstruction code to allow for quantitative SPECT reconstruction. The resulting code was validated using both a physical phantom experiment with spherical objects in a warm background and a realistic anatomical phantom simulation. In the physical phantom study, the authors evaluated the method in terms of quantitative accuracy of activity estimates in the spheres; in the simulation study, the authors evaluated the accuracy and precision of activity estimates from various organs and compared them to results from a previously proposed method.

**Results:** The authors demonstrated excellent agreement between the experimental measurement and Monte Carlo simulation. In the XCAT phantom simulation, the proposed method achieved much better accuracy in the modeling (error in photon counts was  $-1.1\%$ ) compared to a previously proposed method (errors were more than  $20\%$ ); the quantitative accuracy of activity estimates was excellent for all organs (errors were from  $-1.6\%$  to  $11.9\%$ ) and comparable to previously published results for  $^{131}\text{I}$  using the same collimator.

**Conclusions:** The proposed  $^{90}\text{Y}$  bremsstrahlung SPECT reconstruction method provided very accurate estimates of organ activities, with accuracies approaching those previously observed for  $^{131}\text{I}$ . The method may be useful in verifying organ doses for targeted radionuclide therapy using  $^{90}\text{Y}$ .  
© 2012 American Association of Physicists in Medicine. [<http://dx.doi.org/10.1118/1.3700174>]

Key words: Yttrium-90 bremsstrahlung, quantitative SPECT, model-based compensation, Monte Carlo simulation, targeted radionuclide therapy

## I. INTRODUCTION

Targeted radionuclide therapy (TRT) is an established treatment for certain cancers due to its ability to locally and selectively deposit a toxic dose of radiation to cancerous cells.<sup>1</sup> As an essentially pure  $\beta$ -particle emitter, Yttrium-90 ( $^{90}\text{Y}$ ) is one of the most commonly used radionuclides in TRT and has found commercial application in  $^{90}\text{Y}$  Zevalin radioimmunotherapy of indolent B-cell lymphoma and  $^{90}\text{Y}$  microsphere brachytherapy of hepatic malignancies. Due to variability in the delivery of the therapeutic agents to tumors and normal organs, it is often necessary or desirable to perform patient specific treatment planning; a key part of this treatment planning is estimating the distribution of  $^{90}\text{Y}$  at multiple time points.<sup>2</sup> To this end, pretherapy imaging of a planning dose obtained using either a surrogate radionuclide (e.g.,  $^{111}\text{In}$  for Zevalin) or imaging agent (e.g.,  $^{99\text{m}}\text{Tc}$  MAA for  $^{90}\text{Y}$  microspheres brachytherapy) is often performed.<sup>3,4</sup> However, due to differences in distribution of the imaging agents or variations in uptake over time, this imaging may not exactly reflect the distribution of  $^{90}\text{Y}$  during the therapy. Thus, post-therapy dosimetry based on quantitative imaging of the  $^{90}\text{Y}$  distribution may be useful to provide dose confirmation or allow implementation of more rational dose fractionation protocols.<sup>5</sup>

Although  $^{90}\text{Y}$  decay does not result in gamma ray emissions, it does produce bremsstrahlung photons. While these bremsstrahlung photons have been imaged in the past using conventional single photon emission computed tomography (SPECT) reconstruction methods,<sup>6</sup> the quality of the images has been relatively poor. This is because the bremsstrahlung photon energy spectrum is continuous and extends to energies up to 2.3 MeV. The continuous nature means that energy-based scatter rejection is not effective, and thus, there will be substantial numbers of scattered photons in any energy window. The presence of significant numbers of high-energy photons means that septal penetration and scatter, as well as partial deposition in and backscatter behind the crystal, will further degrade image quality and quantitative accuracy.

Recently, Minarik *et al.*<sup>7</sup> demonstrated the feasibility of quantitative  $^{90}\text{Y}$  bremsstrahlung SPECT imaging by modeling the scatter using effective source scatter estimation (ESSE) method<sup>8</sup> and the collimator-detector response (CDR) using a precalculated CDR table obtained from Monte Carlo (MC) simulation. These models were incorporated into an implementation of the ordered subsets-expectation maximization (OS-EM) algorithm.<sup>9,10</sup> This reconstruction method modeled all the image degrading factors including attenuation, scatter and the full CDR (including septal penetration and scatter) using a single energy range (we refer to their method as the single energy range method in the remainder of this paper). More details about the implications of this will become apparent below.

Further, Minarik *et al.*<sup>7</sup> used the SIMIND MC program<sup>11</sup> to simulate  $^{90}\text{Y}$  bremsstrahlung imaging and generate the scatter kernels and CDR table used in the modeling of image degrading factors. The SIMIND code simulated the emission of

bremsstrahlung photons directly by sampling an energy spectrum obtained from simulations using the MCNPX MC program.<sup>12</sup> As will be shown in more detail below, several of the major MC simulation codes including MCNPX seem to underestimate the abundance of high-energy bremsstrahlung photons.<sup>13</sup> Also, the bremsstrahlung emission distance, i.e., the distance between the  $^{90}\text{Y}$  decay location and the bremsstrahlung photon emission location, was not modeled. Together these factors may have limited the accuracy of the MC simulation.

In fact, in the validation of the SIMIND simulation of bremsstrahlung imaging, Minarik *et al.* reported a mismatch between the simulated and experimentally measured projection data: SIMIND underestimated the full width at half maximum (FWHM) and full width at tenth maximum (FWTM) of the line spread function compared to experimentally measured data. This discrepancy may have resulted in reduced accuracy of the scatter kernels and CDR table. In addition, modeling the image degrading factors using a single energy range has limitations due to the continuous and broad energy distribution of bremsstrahlung photons and the energy dependence of the various factors. As a result, the quantitative accuracy of the proposed method might not have been as good as possible.

The aim of this work was to develop and evaluate an improved quantitative  $^{90}\text{Y}$  bremsstrahlung SPECT method to improve the quantitative accuracy of activity estimates for targeted radionuclide therapy dosimetry applications. Since one factor potentially limiting the accuracy was the method used to generate the CDR tables and scatter kernels, we first improved the accuracy of the SIMIND MC simulation by incorporating an improved bremsstrahlung emission energy spectrum and a model of the distance between the  $^{90}\text{Y}$  decay and bremsstrahlung emission locations. Second, we improved the accuracy of modeling object scatter, attenuation, and the CDR through the use of multiple energy ranges to model better the energy dependence of these effects. We evaluated the improvements in the MC code, the forward model of the image formation process, and the quantitative accuracy of the reconstructed images using a combination of physical phantom experiments and realistic MC simulations.

## II. MATERIALS AND METHODS

### II.A. Improvement in quantitative $^{90}\text{Y}$ bremsstrahlung SPECT method

#### II.A.1. Improvement in SIMIND simulation of bremsstrahlung imaging

Rault *et al.* developed a fast simulation method<sup>13</sup> to simulate the emission of  $^{90}\text{Y}$  bremsstrahlung photons using the GEANT4 application for emission tomography (GATE) MC simulation code.<sup>14</sup> Instead of time-consuming simulation of  $\beta$ -particles, the emission of bremsstrahlung photons was simulated directly based on a precalculated bremsstrahlung energy spectrum and probability density functions (PDFs) of the bremsstrahlung emission distance generated using GATE. They computed these PDFs as a function of the bremsstrahlung

energy in 20 keV steps between 0 and 2 MeV. However, even when taking into account this distance effect, they reported a mismatch between simulated and measured point spread functions. They attributed this to errors in the bremsstrahlung energy spectrum generated using GATE and, as a result, used a measured energy spectrum corrected for the detector energy response, including Compton scatter in the detector, obtained with a high-purity germanium (HPGe) detector. Using this energy spectrum to sample energies of the bremsstrahlung photons and the PDFs for the corresponding energies to sample the bremsstrahlung emission distance, they reported a substantial improvement in agreement between the simulation and the measurement.

However, even with these improvements, the GATE code is computationally inefficient when simulating voxelized phantoms such as XCAT phantom,<sup>15</sup> a widely used digital phantom that provides a realistic model of human anatomy. In contrast, as a MC program dedicated to simulating scintillation camera imaging, SIMIND is much faster and computationally more efficient. As a result, we have incorporated similar improvements into SIMIND in order to facilitate evaluation of our proposed method and rapid generation of the requisite CDR tables and scatter kernels.

Figure 1 shows a comparison of the corrected experimental energy spectrum from Rault *et al.* and one simulated using MCNPX. Note that MCNPX substantially underestimated the abundance of photons with energies higher than 500 keV. Similar underestimation has been observed with other MC codes including GATE.<sup>13</sup> This underestimation has important consequences for simulation of bremsstrahlung imaging because down-scatter (photons with energies above a particular energy window that are scattered and detected in that window) and collimator-detector interactions (septal penetration and scatter, partial deposition in the crystal, as well as the backscatter from structures behind the crystal) can result in high-energy photons contributing to projection data in lower

energy windows. As a result, we used the bremsstrahlung energy spectrum estimated by Rault *et al.* as an improved emission energy spectrum in the SIMIND simulation. In addition to bremsstrahlung photons,  $^{90}\text{Y}$  also emits low-abundance prompt gamma photons (1.76 MeV,  $7.8 \times 10^{-5}$  cps/Bq). For completeness, we incorporated the prompt gamma photons into this spectrum; this combination is referred to as the improved spectrum in the remainder of this paper. In particular, energies of emitted photons were sampled from this improved spectrum instead of the energy spectrum generated using MCNPX as used in the original work by Minarik *et al.*

We also incorporated the effects of bremsstrahlung emission distance into SIMIND using a method similar to Rault *et al.* We used GATE to simulate the emission of  $\beta$ -particles from a  $^{90}\text{Y}$  point source in water, the interaction of emitted  $\beta$ -particles with the water, and the generation of bremsstrahlung photons. Bremsstrahlung emission distance histograms were estimated as a function of bremsstrahlung photon energy. We generated histograms in energy ranges with varying widths. At lower energies, we used finer energy spacing because of both the higher abundance of emitted photons and more rapid changes in the distance histograms for lower bremsstrahlung energies. We used 20, 50, 100, and 200 keV energy intervals for bremsstrahlung photons with energies in the ranges of 0–300, 300–500, 500–1000 and 1000–2000 keV, respectively. Sample distance histograms are shown in Fig. 2.

We incorporated these two improvements into the SIMIND simulation of  $^{90}\text{Y}$  bremsstrahlung imaging as follows. First, the  $^{90}\text{Y}$  decay location was sampled within the source volume with a probability proportional to the activity concentration. The photon energy was then sampled from the improved spectrum. The bremsstrahlung emission distance was then sampled from the distance histogram corresponding to the emitted photon's energy. Then, the direction from the  $^{90}\text{Y}$  decay location to the bremsstrahlung emission location

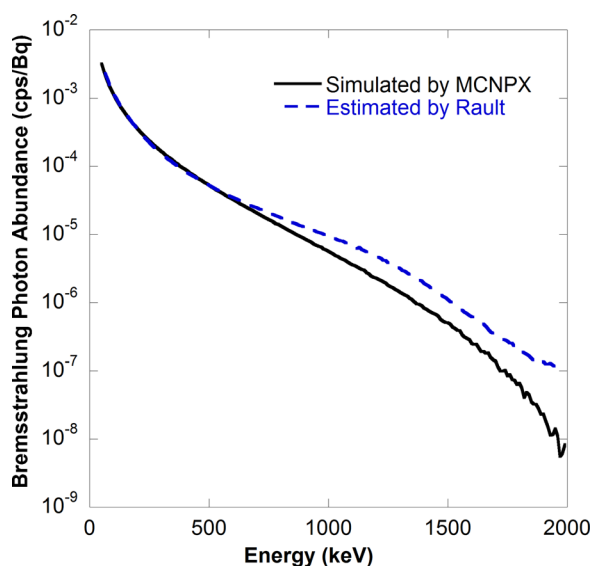


FIG. 1. Energy spectra (50–2000 keV, 10 keV interval) of  $^{90}\text{Y}$  bremsstrahlung photons in water simulated using MCNPX (solid line) and estimated from experimental measurement by Rault *et al.* (dashed line).

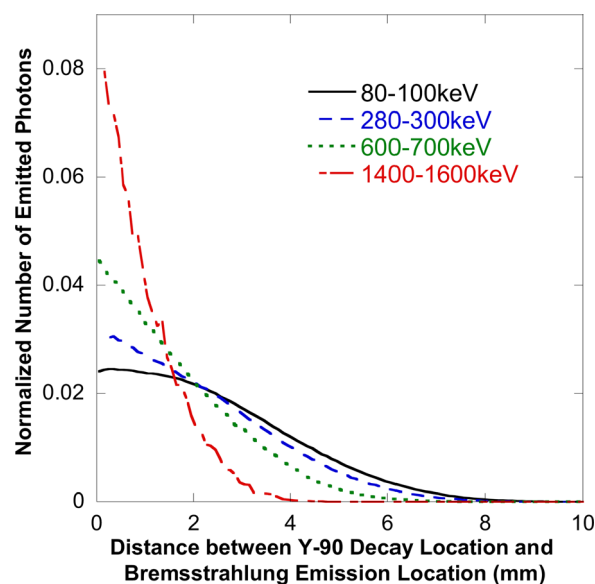


FIG. 2. Sample distance histograms (bin width was 0.1 mm) displayed for four different energies.

was sampled isotropically, and the bremsstrahlung emission location was calculated. Finally, the photon was emitted isotropically from this location, and then propagated through the object and collimator-detector system using the standard radiation transport methods implemented in SIMIND.

### **II.A.2. Multirange method to improve modeling of bremsstrahlung photon image formation**

In addition to improving the scatter kernels and CDR tables by improving the SIMIND bremsstrahlung simulation, we have also developed an improved method to model the image formation process. This is essential since the accuracy of the reconstructed images obtained with iterative reconstruction methods is closely tied to the accuracy of the image formation process modeled in the projector.

*II.A.2.a. Single energy range (SER) method and its limitations.* Modeling the image formation process requires modeling attenuation and scatter of the photons in the patient as well as interactions with the collimator-detector system. In the SER method, Minarik *et al.* modeled attenuation, scatter, and the CDR as constant over the whole energy range. Since all of these image degrading effects are energy dependent, modeling them as constant over the very broad energy range results in limited modeling accuracy.

*Limitations in attenuation modeling.* Attenuation of photons in the patient is modeled in the SER method using a single effective attenuation coefficient computed based on the bremsstrahlung emission energy spectrum inside the acquisition energy window. This approximation is less accurate as the width of the energy window increases due to beam hardening.

*Limitations in scatter modeling.* Both the proposed and SER methods use ESSE to model scatter in the patient. The ESSE method models propagation of photons from their point of origin until their last scatter location in the body, and includes the interactions in the detector but not the collimator. Logically one can divide scatter measured in an energy window into direct- and down-scatter. Both designations refer to photons scattered in the patient and detected in the energy window of interest. Direct-scatter refers in particular to the photons with emission energies inside the window, and down-scatter refers to photons with emission energies above the window. In ESSE, scatter is modeled by computing an effective scatter source using a pair of scatter kernels estimated from MC simulation. These kernels are estimated by MC simulation of a point source with a given emission energy spectrum in the center of a water slab. Photons are propagated through the collimator-detector system until detected. The first kernel represents the average probability that a photon has its last scatter interaction before detection in the energy window of interest at each voxel in the slab. The second kernel represents the average attenuation coefficient of scattered photons after their last scatter event in corresponding voxels. These kernels are used to model scattering in the object via spatially invariant convolution. A correction is included to account for the change in energy after scatter that is based on a Taylor Series

expansion; this expansion is truncated and is most accurate when the change in energy after scattering is small. In the SER method direct- and down-scatter are treated together. Since the energy window used is relatively large and since the energy range of down-scattered photons is even larger, the accuracy of the scatter modeling is limited.

*Limitations in CDR modeling.* Both scattered and unscattered photons are propagated through the collimator-detector system using CDR tables estimated using MC simulations of a point source in air.<sup>16</sup> Since the CDR is a function of energy, the accuracy of the CDR table will depend on how closely the actual energy spectrum of photons incident on the collimator matches the spectrum used in the generation of the CDR table. In the SER method, a single CDR table calculated using the bremsstrahlung emission energy spectrum is used for unscattered and direct- and down-scattered photons. However, due to beam hardening and object scattering, the energy spectrum of these photons is object dependent and, in general, very different from the emission energy spectrum.

Since all of these image degrading effects are energy dependent, it is critical to account for the changes in the energy spectrum in modeling bremsstrahlung photon image formation. The SER method, however, does not account for the changes in the energy spectrum since it treats all different kinds of photons together. To overcome its limitations, we proposed the multiple energy range (MER) method.

*II.A.2.b. MER method.* In the SER method, Minarik *et al.* used a 105–195 keV acquisition window based on considerations about the fraction of primary versus other photons. In the MER method, we selected a 100–500 keV acquisition window based on the trade-off between several factors. First, the overall abundance of bremsstrahlung photons with energies higher than 50 keV is only about 2% in water. Thus, for applications such as  $^{90}\text{Y}$  radioimmunotherapy where the injected activity is modest, there would be relatively few photons emitted. This argues for using as wide an energy window as possible. We selected 100 keV as a lower bound since the fraction of multiple scatter increases dramatically at lower energies and the ESSE scatter model has relatively poor performance for photons with high scatter orders. We selected 500 keV as an upper bound since higher energy photons result in much larger amounts of collimator penetration and scatter, which are also difficult to model accurately and could increase the bias in the activity estimates. We should note that the above energy window was not formally optimized and doing so will be the subject of future work.

Figure 3 shows the MER method schematically. In this context, “multiple energy range” does not refer to the use of multiple acquisition energy windows; on the contrary, a single acquisition window was used (100–500 keV). Instead, it refers to the separate treatment of photons in various energy ranges and in various logical categories during the modeling process. In particular, we separated photons into eight categories based on energy and logical category. Primary photons (i.e., photons not scattered in the body) were separated into four categories according to their emission energies: 0–250, 250–500, 500–1000, and 1000–2000 keV. Scattered

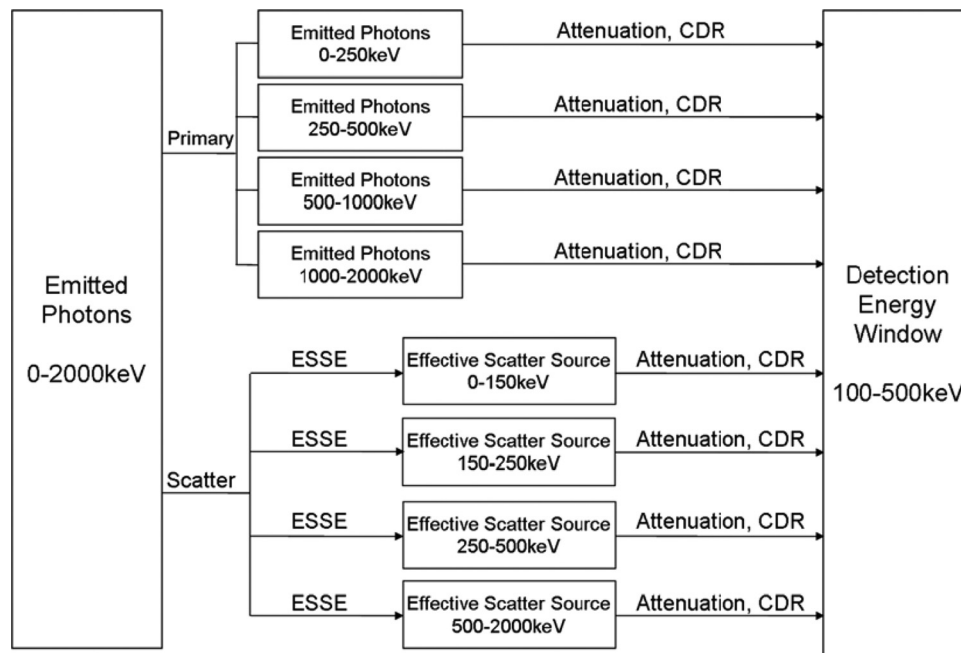


FIG. 3. Schematic of forward projection model used in MER method. Blocks marked "emitted photons" correspond to bremsstrahlung photons emitted in the indicated energy range that exited the body without interacting. Blocks marked "effective scatter source" indicate that ESSE was used to simulate photons having the indicated range of energies after their last scatter event. On each line labeled "Attenuation, CDR" the photons were attenuated using an effective attenuation coefficient appropriate for an appropriate energy spectrum in the energy range indicated in the previous block.

photons were also separated into four categories according to their energies after their last scatter events within the body: 0–150, 150–250, 250–500, and 500–2000 keV. Note that in both cases the energy ranges represent the energy of the photon when it reaches the collimator-detector system. This is different than in the SER method and in previous applications of ESSE using gamma photon emitters where the energy was the energy of emitted photons. In the modeling of primary photons, the attenuation and CDR were modeled for each energy subrange. In the modeling of scattered photons, we computed the effective scatter source using the ESSE scatter kernels in energy subranges based on the energy of scattered photons after their last scatter events in the body; the attenuation and CDR were also modeled for each subrange.

**Attenuation modeling.** For each subrange, we used a different effective attenuation coefficient for primary photons. The effective attenuation coefficient is a function of source depth. In addition, the interactions of primary photons with the detector affect the detection probability for a given energy range (e.g., partial deposition due to Compton scattering in the crystal); as a result, the effective attenuation coefficient is also affected by the detector interactions. To account for the effects of both the source depth and the detector interactions on the effective attenuation coefficient, instead of computing the coefficient directly from the emission energy spectrum, we computed it using MC simulations of a point source at the center of a 15 cm radius cylindrical phantom and in air. We chose 15 cm as a reasonable representative depth considering the average distance primary photons propagate before exiting the body in general. In these simulations, we used the improved spectrum lying in

each subrange and recorded only the number of geometrically collimated primary photons detected in the acquisition window 100–500 keV. The effective attenuation coefficient of water was given by  $(\ln(C_{\text{air}}/C_{\text{phan}}))/15 \text{ cm}^{-1}$ , where  $C_{\text{air}}$  and  $C_{\text{phan}}$  were the detected geometrically collimated primary photon counts.

**Scatter modeling.** The ESSE scatter kernels were calculated from a SIMIND simulation of a point source in the center of a water slab of size  $100 \times 80 \times 80 \text{ cm}^3$ . We used the improved spectrum as an input and recorded photons in subranges based on their energy after their last scatter events in the water phantom.

**CDR modeling.** As discussed above, the CDR depends on the energy spectrum of incident photons, and this energy spectrum changes due to beam hardening and object scattering. To take this into account the input energy spectrum for the CDR table calculation was the spectrum obtained from a simulation of a 20 cm diameter by 30 cm long uniformly emitting water cylinder; in this simulation, photons were emitted with the energy sampled from the improved spectrum, and the energy spectra of primary and scattered photons inside each subrange exiting the phantom were stored and used as the input energy spectra for the CDR table calculation for primary and scattered photons, respectively.

We incorporated the MER method into an OS-EM-based iterative reconstruction algorithm. In the forward projector,<sup>17,18</sup> all the image degrading factors were modeled as illustrated in Fig. 3. In the back-projector, scatter was not modeled and the geometric response function (GRF) was modeled instead of the full CDR (Refs. 19 and 20) in order to improve the convergence rate and reduce computation time.

## II.B. Validation of improved SIMIND simulation of $^{90}\text{Y}$ bremsstrahlung imaging

A comparison between experimental measurements and corresponding simulations was performed using the custom designed rod phantom shown in Fig. 4 in order to validate the improved simulation of  $^{90}\text{Y}$  bremsstrahlung imaging. The rod phantom had an inner diameter of 0.34 cm, and an outer diameter of 2.54 cm, and was filled with a solution of  $^{90}\text{Y}$  up to a length of 10 cm. These dimensions were chosen such that the distance from the outer boundary of the compartment containing the  $^{90}\text{Y}$  solution to the outer boundary of the phantom was 1.1 cm, which is the maximum range of  $^{90}\text{Y}$   $\beta$ -particles in water. In this way, nearly all  $\beta$ -particles were stopped, but the attenuation of the bremsstrahlung photons was still relatively small. The phantom was imaged using a dual-camera Philips Precedence SPECT/CT system with a high-energy general-purpose (HEGP) collimator. The crystal thickness was 9.525 mm and the acquisition energy window used was 100–500 keV. The distance between the center of the line source and the camera face was 15.8 cm. The projection image at each view had  $128 \times 128$  pixels and the pixel size was 4.664 mm. Background counts were measured and subtracted from the phantom projections. Simulations were conducted with the same system geometry and imaging parameters as in the measurement using the improved SIMIND, GATE, and standard SIMIND (using the emission energy spectrum from MCNPX and no bremsstrahlung emission distance model) codes. The compartment behind the crystal was modeled as a slab made of  $\text{SiO}_2$  with density of  $2.6 \text{ g/cm}^3$  and thickness of 6 cm. We modeled a Gaussian energy resolution with a FWHM of 9.5% at 140 keV and an intrinsic spatial resolution of 3.4 mm, both with an energy dependence of  $1/\sqrt{E}$ , where  $E$  represents the deposited energy. In the GATE simulation, the emission and propagation of both  $\beta$ -particles and bremsstrahlung photons were simulated. Profiles through the phantom projections averaged over ten consecutive rows of pixels in the middle of the line source were compared between the measurement and the simulations.

## II.C. Evaluation of the MER method

Both physical phantom and simulated XCAT phantom experiments were conducted to evaluate the performance of the MER method. The physical phantom experiment provides the benchmark in accuracy of modeling of the physics and camera; the XCAT phantom study provides more realistic modeling of patient anatomy, eliminates errors in measure-

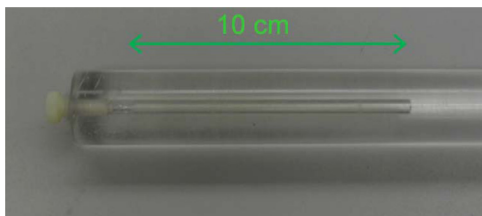


Fig. 4. Custom designed rod phantom used as a line source for MC simulation validation and sensitivity measurements.

ment of activity and in definition of object volumes-of-interest (VOIs), and facilitates estimation of precision. In the physical phantom experiment, we evaluated the quantitative accuracy of activity estimates from the MER and SER methods; in the XCAT phantom simulation, we compared the MER method to the SER method in terms of the errors in projection modeling and activity estimates. In both cases we also included a comparison to the results from OS-EM with attenuation compensation alone to provide a basis for comparing to what one might obtain with typical commercial software. All the following simulations were conducted using the improved version of SIMIND.

### II.C.1. Physical phantom experiment

An elliptical phantom with three spheres of different sizes was used in the experimental evaluation (see Fig. 5). The activity was uniformly distributed in each compartment. To minimize the adsorption of  $^{90}\text{Y}$  on the walls of the phantom we used a buffer solution containing ethylenediaminetetraacetate (EDTA).<sup>21</sup> For large and medium spheres, the sphere-to-background activity concentration ratio was about 10:1; for the small sphere, the ratio was about 20:1. The activity in each compartment was measured using a Capintec dose calibrator with a dial setting of 55 and a readout scale factor of 10, as suggested by Zimmerman *et al.*,<sup>22</sup> and using the same type of syringes with the same solution volume and with the syringe at the same position in the dose calibrator. The total activities in the background, large, medium, and small spheres were 1657.7, 121.9, 27.4, and 5.9 MBq, respectively. The imaging system, collimator and acquisition window were the same as used in the rod phantom experiment. Projections were acquired at 128 views over  $360^\circ$  in a  $128 \times 128$  matrix with a pixel size of 4.664 mm. The imaging time was 45 s per projection view. CT images were acquired in connection with the SPECT measurements for use in attenuation and scatter compensation. The manufacturer's software was used to rescale the CT images to represent the attenuation at 100 keV and to register the CT images with the SPECT images. Nonuniformity correction was performed using intrinsic



Fig. 5. Elliptical phantom used in physical phantom experiments showing three spheres of different sizes.

flood-field images acquired for both detectors using the  $^{90}\text{Y}$  rod source phantom.

The images were reconstructed with up to 400 iterations of 16 subsets per iteration using the OS-EM algorithm with attenuation compensation alone (representing what could be achieved with typical commercial software), the MER and the SER methods. The dimensions of the reconstructed images were  $128 \times 128 \times 128$  and the voxel size was 4.664 mm. For the MER method, the CT images were rescaled to generate the attenuation map for each energy subrange such that attenuation coefficient for water in this map was equal to the effective attenuation coefficient, calculated as described above, for the corresponding energy subrange.

Although we directly measured the activity in each sphere, knowledge of the sphere volume was useful in defining VOIs for activity quantification. We used an electronic balance with a precision of 1 mg to measure the masses of individual spheres when they were dry and were full of solution. Then, we calculated the difference of the masses and divided by the density of water to give the volume of each sphere. The resulting volumes were 89.610, 19.009, and  $2.004 \text{ cm}^3$ , respectively. The corresponding inner diameters were 5.5, 3.3, and 1.5 cm, respectively. The VOIs for the three spheres were defined based on the SPECT image so that the volumes in the VOIs were consistent with the measured volumes.

After reconstruction, the voxel values in the SPECT image were in units of geometrically collimated primary photons per voxel. To convert the sum of voxel values inside the VOIs to activity we needed a measure of camera system sensitivity (in cps/MBq) for geometrically collimated primary photons. The rod phantom (Fig. 4) filled with  $^{90}\text{Y}$  solution having an activity of 263 MBq was imaged from one view for 5 min to measure the sensitivity. Since it is not possible to directly measure the number of geometrically collimated primary photons from the image, a corresponding simulation was conducted using SIMIND. The ratio of the total counts in the measured data to that in the simulated data was calculated in an ROI covering the center of the phantom. This ratio was then multiplied by the sensitivity for geometrically collimated primary photons obtained from the SIMIND simulation to determine the camera system sensitivity, which was 1.20 cps/MBq.

### II.C.2. XCAT phantom experiment

An XCAT phantom with a  $^{90}\text{Y}$  activity distribution based on patient  $^{111}\text{In}$  Zevalin data was used to evaluate the MER method. We simulated the same dual-camera SPECT system as in the physical phantom experiment, a 30 min total acquisition time, and a total activity of 2960 MBq, a total activity representative of what might be used in a myeloablative therapy regimen. Data were simulated at 128 projection views over  $360^\circ$  and the matrix size for each projection view was  $128 \times 128$  with a pixel size of 4.664 mm. Both 100–500 and 105–195 keV acquisition windows were simulated. We simulated a total of  $10^{12}$  photon emissions using the variance reduction techniques available in SIMIND (including perpetual

propagation, forced detection, and delta tracking in the collimator) to generate low-noise projection data. The noise in the resulting projections was very low (negligible compared to a realistic noise level) and not Poisson distributed due to the variance reduction. To allow studying the effects of noise, we scaled the projections to a realistic mean count level based on the activity and acquisition duration and then simulated 50 Poisson noise realizations using a pseudorandom number generator.

To verify the modeling accuracy for the image degrading factors obtained using the MER method, projections for each of the eight photon categories were estimated separately using the true activity distribution as an input; the resulting projections were compared to corresponding ones generated with SIMIND. We also compared the modeling accuracy from the MER method to that from the SER method.

The images were reconstructed with up to 200 iterations of 16 subsets per iteration using the OS-EM algorithm with attenuation compensation alone, the MER, and the SER methods. A uniform activity distribution was used as the initial estimate in all cases. The dimension of the reconstructed images was  $128 \times 128 \times 128$  and the voxel size was 4.664 mm. For the MER method, the effective mass attenuation coefficients were estimated for water in the four primary photon energy subranges and for bone in the 250–500 keV subrange using SIMIND simulations. The attenuation map for the 250–500 keV subrange was generated by multiplying the mass density map produced by the XCAT phantom code by the effective mass attenuation coefficient for 250–500 keV for either bone or water depending on whether the density value exceeded  $1.2 \text{ g/cm}^3$ . For the other energy subranges the attenuation maps were calculated by multiplying the attenuation map for the 250–500 keV subrange by the ratio of the effective attenuation coefficient for water in the sub-range to that for 250–500 keV.

The total activities in the individual organs were estimated from the reconstructed images and the true organ VOIs. Note that the blood vessels were simulated with different activities than the other organs in the XCAT phantom used in this study. However, when quantifying activities the regions corresponding to blood vessels inside each organ were included in the VOI of that organ since in practice it would be difficult or impossible to obtain accurate VOIs for the blood vessels. For images reconstructed from data without added Poisson noise, the percent errors in activity estimates for the individual organs were calculated based on the true organ activities. For data with added Poisson noise, mean and standard deviation (s.d.) of percent errors in organ activity estimates, and percent root mean squared error (percent RMSE) of organ activity estimates were calculated over 50 Poisson noise realizations. The percent errors in activity estimates were calculated as:

$$\text{Percent error} = (\text{Estimated} - \text{True}) / \text{True} \times 100\%$$

$$\text{Percent RMSE} = \sqrt{\frac{1}{50} \sum_{i=1}^{50} (\text{Estimated}_i - \text{True})^2} / \text{True} \times 100\%$$



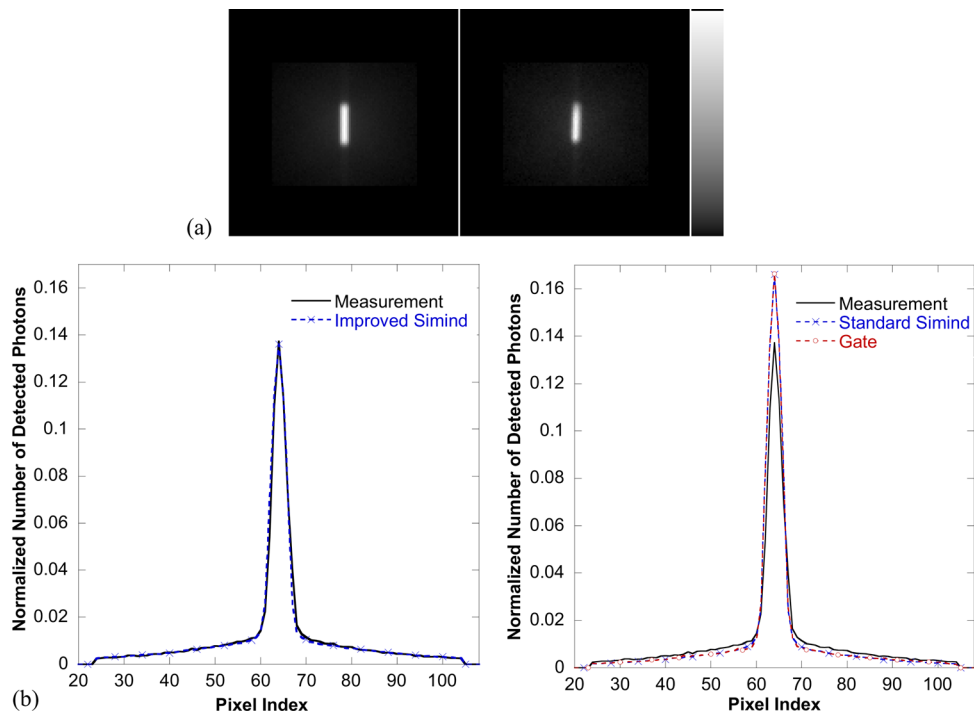


FIG. 6. (a) Projection of the rod phantom simulated using the improved SIMIND (left) and measured (right). (b) Ten pixel wide horizontal profiles through the middle of the rod phantom images in (a). The profiles were normalized to unit total area and enough photons were simulated so that the noise in the profiles was very small.

### III. RESULTS

#### III.A. Validation of improved SIMIND simulation

Figure 6 shows both the simulated and the measured projection data for the rod phantom and 10 voxel wide line

profiles along the horizontal direction in the middle of the rod phantom. The profiles were normalized so that the area under each profile was 1. From the comparison of the profiles, we can see that the data simulated using the improved SIMIND was in excellent agreement with the measured data.

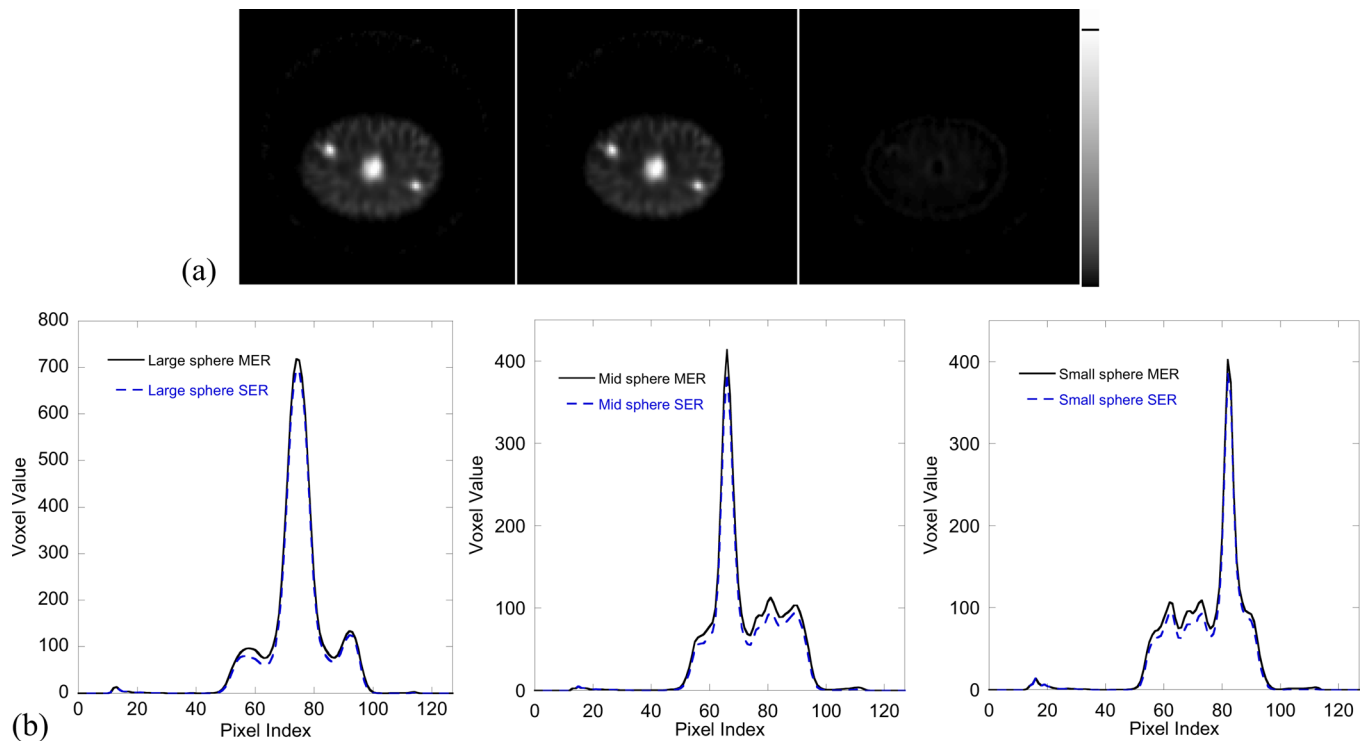


FIG. 7. (a) Central slice of the reconstructed image obtained after ten iterations (16 subsets per iteration) of OS-EM using the MER (left) and SER (middle) method and the difference image (right) for the physical phantom experiment. (b) Fifteen pixel wide vertical profiles through the center of each sphere in (a).

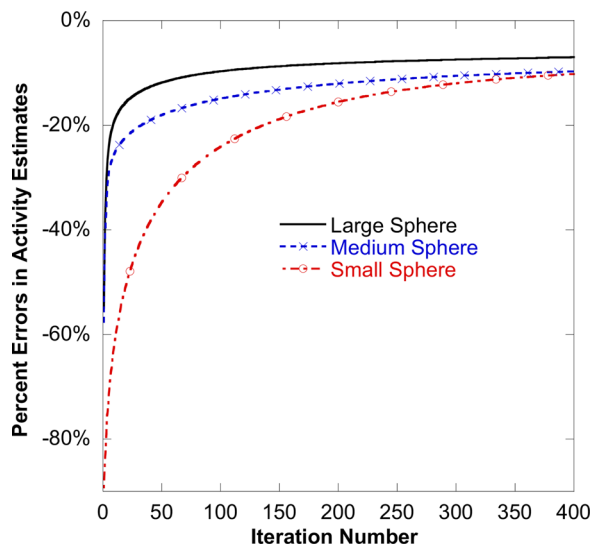


FIG. 8. Percent errors in activity estimates as a function of the number of OS-EM iterations (16 subsets per iteration) for each of the three spheres using the MER method. Percent error = (Estimated Activity – True Activity)/True Activity  $\times$  100%.

The data simulated with both the standard SIMIND and GATE codes agreed well with each other but did not agree well with the measured data. In particular, they had a sharper peak and reduced tails. One explanation of this is underestimation of high-energy photon abundance by the  $\beta$ -particle simulations in MCNPX and GATE. This explanation is consistent with similar observations by Rault *et al.*: “This underestimation could be attributed to either an incorrect  $^{90}\text{Y}$  beta spectrum or deficiencies in the sampling of the high-energy portion of the bremsstrahlung photon energy spectrum in the GEANT4 code.”<sup>13</sup>

### III.B. Physical phantom experiment

Figure 7(a) shows the central slice of the reconstructed phantom image obtained using the MER and SER methods and the difference image. Figure 7(b) shows the fifteen pixel wide vertical profiles through the center of each sphere in (a). It demonstrates the good image quality that can be obtained. In particular, the three spheres are clearly visualized. Figure 8 shows the percent errors in the activity estimates for the spheres as a function of iteration number for the MER method, and Table I gives the values of the percent errors after 400 iterations for the MER and SER methods and attenuation compensation alone. From these we see that the MER method achieved the best quantitative accuracy among the three methods. As will be shown in the following XCAT phantom experiment, for realistic human anatomy, the improvement in quantita-

TABLE I. Percent errors in activity estimates<sup>a</sup> from physical phantom experiment.

	Large sphere (%)	Medium sphere (%)	Small sphere (%)
MER	-7.0	-9.7	-10.2
SER	-9.4	-12.3	-12.8
Attenuation compensation	90.6	27.0	-39.8

<sup>a</sup>After 400 iterations of 16 subsets per iteration.

tive accuracy achieved by the MER method compared to the SER method was greater than that for the relatively simple and clinically unrealistic structure of the physical phantom.

### III.C. XCAT phantom simulation

#### III.C.1. Modeling accuracy for the image degrading factors

Table II shows the errors in estimates of the total projection counts for each photon category with the MER method. Table III shows a comparison of errors in the estimated total counts for the MER method using the 100–500 keV window and the SER method using both the 100–500 and 105–195 keV windows. Note that the error from the MER method was very small, and the SER method substantially overestimated the total counts, with the error, as expected, being somewhat better for the narrow energy window than the wide one. Figure 9 shows projection images and profiles through them for the MC simulated images and images estimated using the MER and SER methods. This confirms that the MER method substantially improved the modeling accuracy.

#### III.C.2. Quantitative accuracy and precision of organ activity estimates

Figure 10(a) shows coronal slices of the attenuation map, activity distribution and images reconstructed using the MER and SER methods and attenuation compensation alone. Note the substantial improvement in image quality compared to attenuation compensation alone. Figure 10(b) shows vertical profiles through the center of the liver in the images reconstructed using the MER and SER methods. From the profiles, we can see that the SER method underestimated the activity compared to the results from the MER method.

Table IV shows the percent errors in organ activity estimates for the data without added noise after 200 iterations of 16 subsets per iteration for the MER and SER methods and for attenuation compensation alone. These data demonstrate the vast improvement in accuracy obtained using the SER or MER methods compared to standard reconstruction. They

TABLE II. Errors in photon counts for various photon categories obtained using the MER method.

Category	Primary 0–250	Primary 250–500	Primary 500–1 k	Primary 1–2 k	Scatter 0–150	Scatter 150–250	Scatter 250–500	Scatter 500–2 k	Total
Error <sup>a</sup> (%)	0.00	0.01	0.22	-0.25	0.26	-0.16	-0.16	-1.03	-1.10

<sup>a</sup>Error = (Estimated counts – Simulated counts)/total simulated counts  $\times$  100%.

TABLE III. Percent errors in total counts for various modeling methods and energy windows.

Method	MER 100–500 keV	SER 100–500 keV	SER 105–195 keV
Error <sup>a</sup> (%)	–1.1	23.2	21.4

<sup>a</sup>Error = (Estimated counts – Simulated counts)/Simulated counts  $\times$  100%.

also demonstrate the improvement in accuracy provided by MER compared to SER.

Figure 11 shows plots of the percent error and RMSE of the liver activity estimates obtained using the various methods and energy windows as a function of the iteration number from the ensemble of noisy projection data. For all the methods, the accuracy improved with iteration and the precision (indicated by the error bars) worsened. The RMSE data indicate that 50 iterations are sufficient to achieve near-optimal results. Similar observations were made for the other organs. Based on this, we used 50 iterations in the precision evaluation presented below.

Table V shows the mean and standard deviation of the percent errors in the organ activity estimates for the SER and MER methods estimated from the ensemble of noisy projection data. These data confirm the improvement in accuracy

provided by the MER method. They also demonstrate that both methods and, for the SER method, both energy windows provided similar precision.

#### IV. DISCUSSION

As discussed above, a major motivation for the MER method and an explanation for the improved modeling accuracy is its improved modeling of beam hardening and the effect it has on modeling the energy spectrum of photons exiting the body and the CDR. To illustrate this, we generated the energy spectra of primary photons incident on the collimator after passing through 0, 5, and 20 cm of water. The results are shown in Fig. 12. Note the substantial difference in the relative number of photons at low and high energies. Since the SER method assumes the same incident energy spectrum for all depths, it is clear that errors in the modeling of various effects will result. In the MER method the change in energy spectrum as a function of source depth is reduced by the use of multiple energy ranges in the modeling. This is a major reason that the MER method achieved such a substantial reduction in modeling error and resulting improved accuracy of the reconstructed images.

As noted above, with the MER method the error in the total counts was as small as 1.1%. The agreement in count

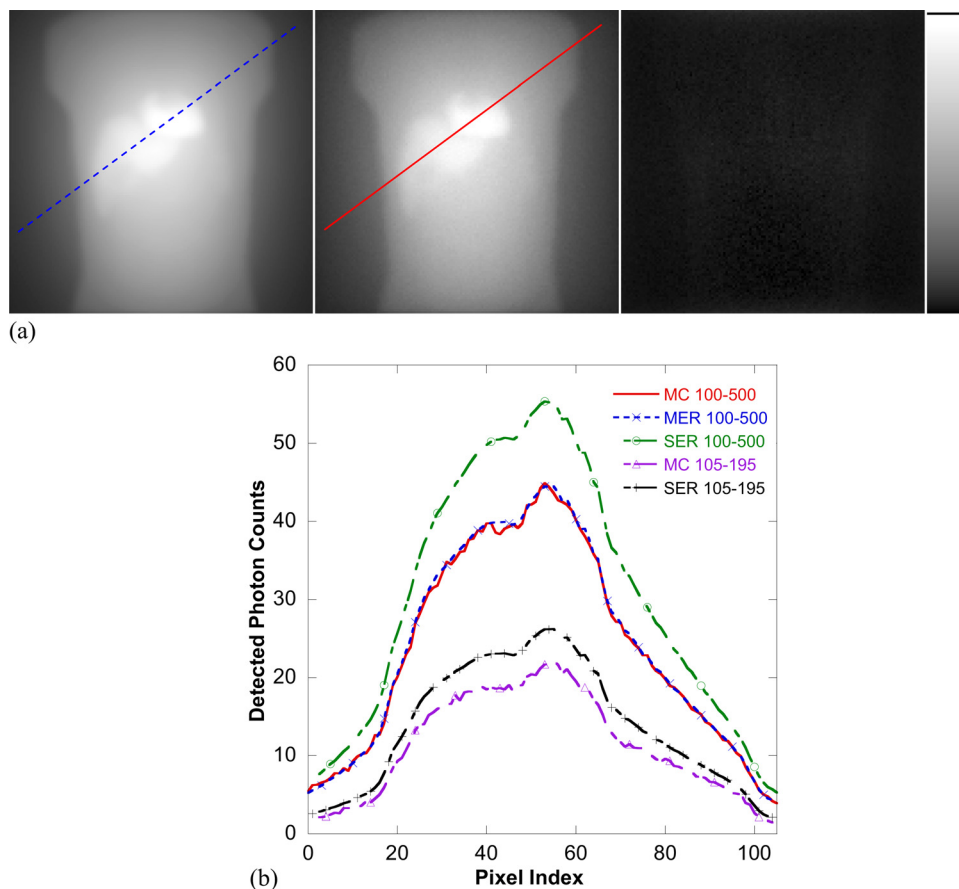


FIG. 9. (a) Anterior projection view estimated using the MER method (left), MC simulated (middle), and the difference image (right) all shown on the same gray scale; (b) Profiles through projections at the position indicated by lines in (a) of MC simulated images and images estimated using the MER and SER methods for the 100–500 and 105–195 keV energy windows, as indicated in the legend.

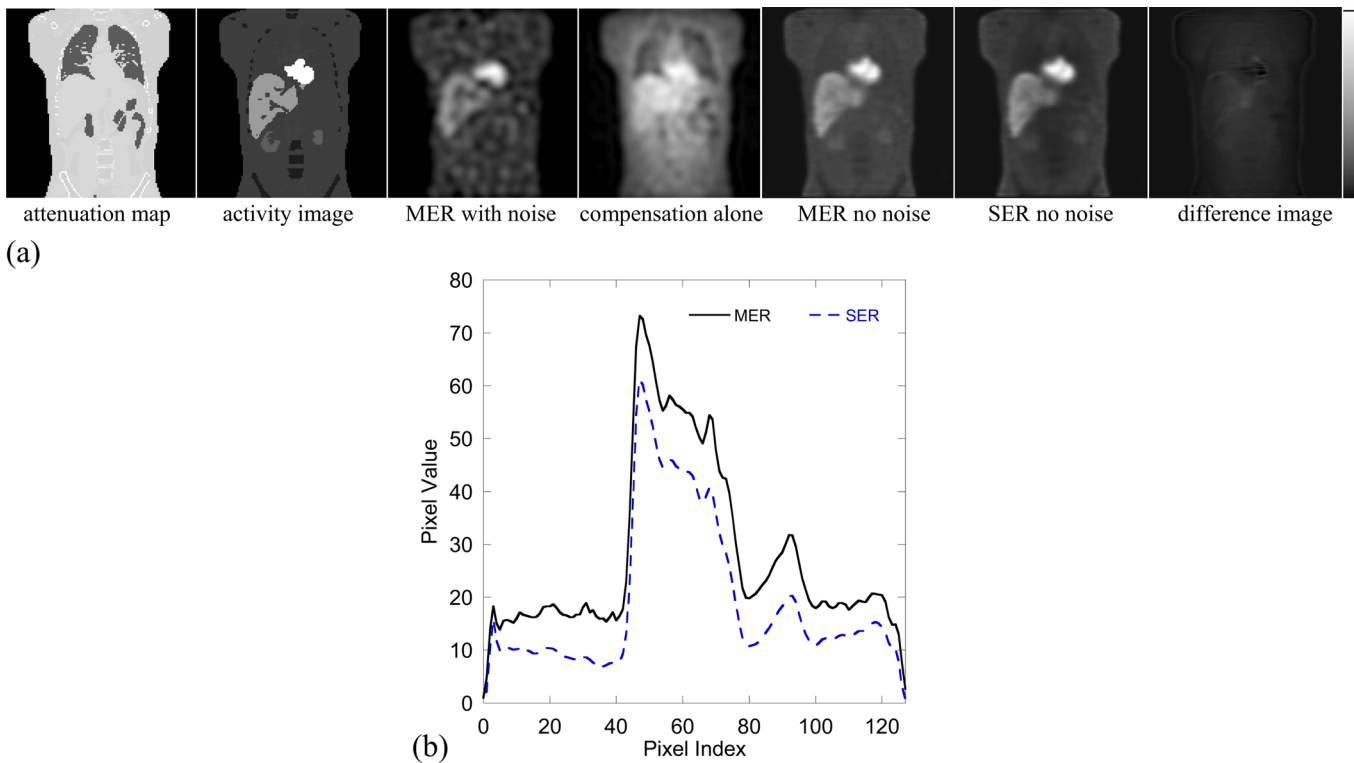


FIG. 10. (a) Sample coronal slices of (left to right) the attenuation map, activity distribution, images reconstructed using the MER method and attenuation compensation alone from data with noise corresponding to 2960 MBq total activity and 30 min imaging time, and images reconstructed using the MER and SER 100–500 keV from data without added noise and the difference image. The reconstructed images were obtained using ten iterations with 16 subsets per iteration and the third and fourth images were filtered using a 3D Butterworth postreconstruction filter with order 8 and cutoff  $0.11 \text{ pixels}^{-1}$ . (b) Vertical profiles through the center of the liver in the fifth and sixth images in (a).

TABLE IV. Percent errors in organ activity estimates<sup>a</sup> for data w/o added noise.

	Lung (%)	Spleen (%)	Kidneys (%)	Liver (%)	Heart (%)
MER 100–500 keV	11.9	–5.9	–3.2	–1.6	–2.4
SER 100–500 keV	–27.0	–11.3	–29.6	–15.3	–8.8
SER 105–195 keV	–21.1	–9.1	–25.5	–12.8	–7.1
attenuation compensation	324.4	121.5	400.9	254.1	133.8

<sup>a</sup>After 200 iterations of 16 subsets per iteration.

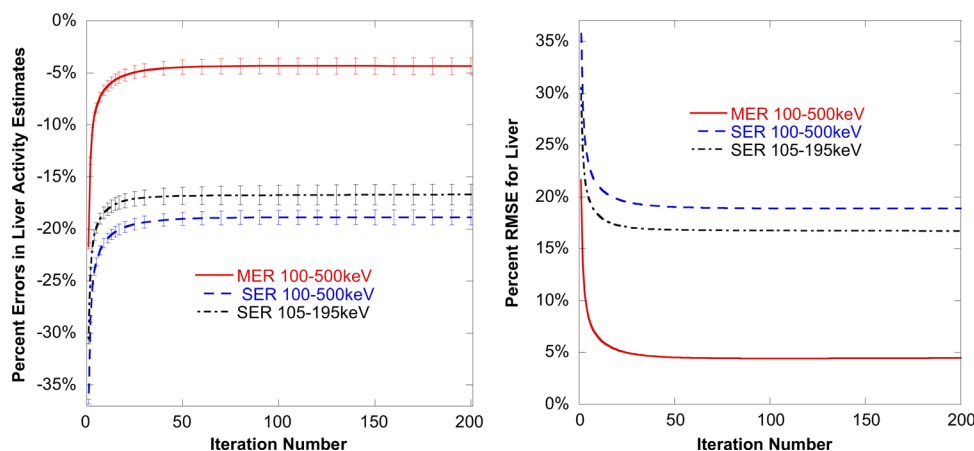


FIG. 11. Mean and standard deviation of percent errors (left) and percent RMSE (right) of the activity estimates for the liver from 50 Poisson noise realizations as a function of the number of OS-EM iterations (16 subsets per iteration) for the MER method and SER method using data acquired in the energy windows indicated in the legend. The error bars in the left figure represent the standard deviations.

TABLE V. Mean and standard deviation of percent errors in organ activity estimates<sup>a</sup> for simulated noisy data.

	Lung (%)	Spleen (%)	Kidneys (%)	Liver (%)	Heart (%)
MER 100–500 keV	(10.2 ± 2.1)	(−11.9 ± 2.3)	(−6.4 ± 5.0)	(−4.5 ± 0.7)	(−5.8 ± 0.9)
SER 100–500 keV	(−28.0 ± 1.9)	(−18.9 ± 2.2)	(−33.4 ± 4.4)	(−19.0 ± 0.6)	(−12.8 ± 0.8)
SER 105–195 keV	(−22.0 ± 1.9)	(−17.2 ± 2.5)	(−28.8 ± 4.8)	(−16.8 ± 0.8)	(−11.5 ± 1.6)

<sup>a</sup>(Mean ± s.d.) from 50 Poisson noise realizations after 50 iterations of 16 subsets per iteration.

distributions in the estimated and MC simulated projections was also very good. However, the errors in organ activity estimates were larger than the modeling errors. We believe that the residual errors result from partial volume effects due to the inability to completely recover the image resolution.<sup>23</sup> The data on the order of the relative errors in the organ activity estimates confirm this. From Table IV, we can see that the activities of the liver, heart, kidneys and spleen were underestimated, with larger errors being seen in smaller organs. This is consistent with the residual errors being due to spill-out of activity. The overestimation of lung activity is also consistent with this: the lung activity was overestimated due to spill-in from surrounding organs since it was in close proximity to organs, such as the heart and liver, that had much higher relative activities. For the SER method, however, the modeling errors for image degrading factors seem to have been a more important factor limiting the accuracy in activity estimates than partial volume effects.

To give a frame of reference for the accuracy of the reconstructed images, we compared the quantitative accuracy for  $^{90}\text{Y}$  to results of a previous simulation study for  $^{131}\text{I}$  using the same collimator. The reconstructions for that study included compensation for all image degrading factors including down-scatter from high-energy photons.<sup>24</sup> Despite the fact that there were differences in organ uptake and organ volumes between the two studies, the accuracies

achieved for quantitative  $^{90}\text{Y}$  bremsstrahlung SPECT were comparable to those for quantitative  $^{131}\text{I}$  SPECT. For example, for the heart and liver, respectively, the errors for  $^{90}\text{Y}$  vs  $^{131}\text{I}$  were  $-2.4\%$  vs  $-4.4\%$  and  $-1.6\%$  vs  $-3.2\%$ . The situation for the lungs is more complicated (the errors were  $11.9\%$  for  $^{90}\text{Y}$  vs  $-4.7\%$  for  $^{131}\text{I}$ ) since the errors for the lungs resulted from both spill-in of activity from the liver and heart and spill-out of activity from the lungs. For the  $^{90}\text{Y}$  study, surrounding organs such as the heart and liver had larger activity concentrations relative to the lungs than for the  $^{131}\text{I}$  study (e.g., the heart-to-lungs activity concentration ratios were 8.6 for  $^{90}\text{Y}$  vs 3.1 for  $^{131}\text{I}$ ). Thus, the amount of spill-in would be greater for  $^{90}\text{Y}$ , explaining the overestimation of the lung activity. In any event, the errors for  $^{90}\text{Y}$  using the MER method were comparable to those for  $^{131}\text{I}$  with full compensation, especially compared to the errors obtained using the SER method or attenuation compensation alone.

The CPU times per iteration for the MER and SER methods on a single core of an Intel Xeon E5410 (2.33 GHz) CPU running Linux were 45.6 and 9.3 min, respectively. No special effort was made to optimize the code nor was it parallelized. In the current code, the computations for each energy range are performed independently, resulting in some redundant calculations that could be removed. Further, these calculations could be readily parallelized to take essentially the same time as the SER method. However, since ten iterations were sufficient to achieve near-optimum performance (see Fig. 11), even with the current code the computation time may not be a major impediment to clinical translation of the MER method.

## V. CONCLUSIONS

In this work, we have developed an improved quantitative  $^{90}\text{Y}$  bremsstrahlung SPECT reconstruction method. The method is based on more accurate modeling of the various image degrading factors. Improvements in the model included enhancements to the SIMIND bremsstrahlung simulation that was used to estimate scatter kernels and collimator-detector response tables used in the method, as well as better modeling of the energy dependence of these effects through the use of multiple energy ranges. The SIMIND bremsstrahlung simulation was improved by incorporating both an improved emission energy spectrum and a model of the distance between  $^{90}\text{Y}$  decay location and bremsstrahlung photon emission location. The reconstruction method was evaluated using both a physical phantom experiment and an XCAT phantom simulation. The evaluation experiments showed

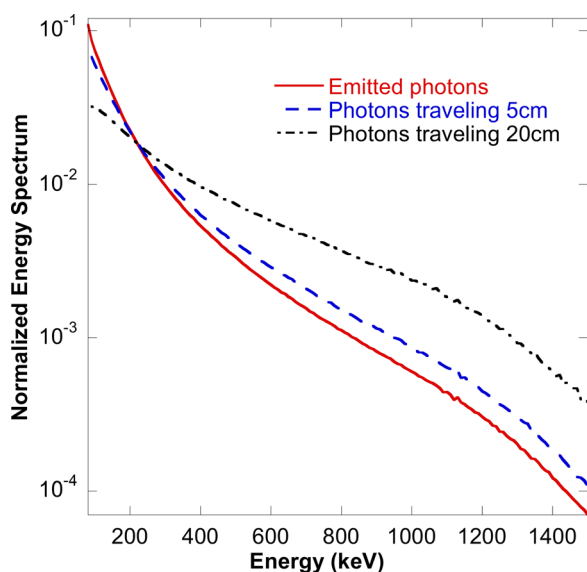


FIG. 12. SIMIND simulated  $^{90}\text{Y}$  bremsstrahlung energy spectrum of primary photons after passing through 0, 5, and 20 cm of water, respectively. The spectra were normalized to have the same total area over the energy range 80–1500 keV.

more accurate modeling of the image formation process than previous methods as well as a resulting improvement in the accuracy of organ activity estimates obtained from reconstructed images. The accuracy of the resulting organ activity estimates were similar to those previously obtained with <sup>131</sup>I using the same collimator-detector system and a similar phantom and activity distribution.

## ACKNOWLEDGMENT

This work was supported by Public Health Service Grant No. R01-CA109234. The content of this work is solely the responsibility of the authors and does not necessarily represent the official view of the PHS or its various institutes.

<sup>a)</sup> Author to whom correspondence should be addressed. Electronic mail: xrong1@jhu.edu

<sup>1</sup>T. Stigbrand, J. Carlsson, G. P. Adams, D. Eriksson, K. Riklund, L. Johansson, F. Y. Frejd, M. d. Jong, S. M. Verwijnen, M. d. Visser, D. J. Kwekkeboom, R. Valkema, E. P. Krenning, V. Tolmachev, G. Sgouros, D. Josten, and R. H. Larsen, *Targeted Radionuclide Tumor Therapy* (Springer Science+Business Media, New York, 2008).

<sup>2</sup>G. Sgouros, E. Frey, R. Wahl, B. He, A. Prideaux, and R. Hobbs, "Three-dimensional imaging-based radiobiological dosimetry," *Semin. Nucl. Med.* **38**, 321–334 (2008).

<sup>3</sup>W. A. Dezam, J. T. Cessna, L. A. DeWerd, W. Z. Feng, V. L. Gates, J. Halama, A. S. Kennedy, S. Nag, M. Sarfaraz, V. Sehgal, R. Selwyn, M. G. Stabin, B. R. Thomadsen, L. E. Williams, and R. Salem, "Recommendations of the American Association of Physicists in Medicine on dosimetry, imaging, and quality assurance procedures for (90)Y microsphere brachytherapy in the treatment of hepatic malignancies," *Med. Phys.* **38**, 4824–4845 (2011).

<sup>4</sup>S. Nag, A. Kennedy, R. Salem, R. Murthy, A. J. McEwan, C. Nutting, A. Benson, J. Espot, J. I. Bilbao, R. A. Sharma, J. P. Thomas, and D. Coldwell, "Recommendations for radioembolization of hepatic malignancies using yttrium-90 microsphere brachytherapy: A consensus panel report from the Radioembolization Brachytherapy Oncology Consortium," *Int. J. Radiat. Oncol.* **68**, 13–23 (2007).

<sup>5</sup>A. Al-Nahhas, N. Tehranipour, R. Canelo, G. Stamp, K. Woo, P. Tait, and P. Gishen, "Concordant F-18FDG PET and Y-90 bremsstrahlung scans depict selective delivery of Y-90-microspheres to liver tumors: Confirmation with histopathology," *Clin. Nucl. Med.* **32**, 371–374 (2007).

<sup>6</sup>R. Mansberg, N. Sorensen, V. Mansberg, and H. V. D. Wall, "Yttrium-90 bremsstrahlung SPECT/CT scan demonstrating areas of tracer/tumor uptake," *Eur. J. Nucl. Med. Mol. Imaging* **34**, 1887 (2007).

<sup>7</sup>D. Minarik, K. Sjogreen Gleisner, and M. Ljungberg, "Evaluation of quantitative (90) Y SPECT based on experimental phantom studies," *Phys. Med. Biol.* **53**, 5689–5703 (2008).

<sup>8</sup>E. C. Frey and B. M. W. Tsui, "A new method for modeling the spatially-variant, object-dependent scatter response function in SPECT," *IEEE Nuclear Science Symposium*, Vol. 2 (IEEE, Anaheim, CA, 1996), pp. 1082–1086.

<sup>9</sup>K. Lange and R. Carson, "EM reconstruction algorithms for emission and transmission tomography," *J. Comput. Assist. Tomogr.* **8**, 306–316 (1984).

<sup>10</sup>H. M. Hudson and R. S. Larkin, "Accelerated image-reconstruction using ordered subsets of projection data," *IEEE Trans. Med. Imaging* **13**, 601–609 (1994).

<sup>11</sup>M. Ljungberg and S.-E. Strand, "A Monte Carlo program for the simulation of scintillation camera characteristics," *Comput. Methods Programs Biomed.* **29**, 257–272 (1989).

<sup>12</sup>J. S. Hendricks, *MCNPX* (Los Alamos National Laboratory, Los Alamos, 2005).

<sup>13</sup>E. Rault, S. Staelens, R. Van Holen, J. De Beenhouwer, and S. Vandenberghe, "Fast simulation of yttrium-90 bremsstrahlung photons with GATE," *Med. Phys.* **37**, 2943–2950 (2010).

<sup>14</sup>C. Morel, S. Jan, G. Santin, D. Strul, S. Staelens, K. Assie, D. Autret, S. Avner, R. Barbier, M. Bardies, P. M. Bloomfield, D. Brasse, V. Breton, P. Bruyndonckx, I. Buvat, A. F. Chatzioannou, Y. Choi, Y. H. Chung, C. Comtat, D. Donnarieix, L. Ferrer, S. J. Glick, C. J. Groiselle, D. Guez, P. F. Honore, S. Kerhoas-Cavata, A. S. Kirov, V. Kohli, M. Koole, M. Krieguer, D. J. van der Laan, F. Lamare, G. Largeron, C. Lartizien, D. Lazaro, M. C. Maas, L. Maigne, F. Mayet, F. Melot, C. Merheb, E. Pennacchio, J. Perez, U. Pietrzyk, F. R. Rannou, M. Rey, D. R. Schaart, C. R. Schmidlein, L. Simon, T. Y. Song, J. M. Vieira, D. Visvikis, R. V. de Walle, and E. Wieers, "GATE: A simulation toolkit for PET and SPECT," *Phys. Med. Biol.* **49**, 4543–4561 (2004).

<sup>15</sup>W. P. Segars, G. Sturgeon, S. Mendonca, J. Grimes, and B. M. W. Tsui, "4D XCAT phantom for multimodality imaging research," *Med. Phys.* **37**, 4902–4915 (2010).

<sup>16</sup>W. T. Wang, E. C. Frey, B. M. W. Tsui, C. Tocharoenchai, and W. H. Baird, "Parameterization of Pb c-ray contamination in simultaneous Tl-201 and Tc-99m dual-isotope imaging," *IEEE Trans. Nucl. Sci.* **49**, 680–692 (2002).

<sup>17</sup>G. L. Zeng, Y. L. Hsieh, and G. T. Gullberg, "A Rotating and warping projector backprojector for fan-beam and cone-beam iterative algorithm," *IEEE Trans. Nucl. Sci.* **41**, 2807–2811 (1994).

<sup>18</sup>E. C. Frey, Z. W. Ju, and B. M. W. Tsui, "A fast projector-backprojector pair modeling the asymmetric, spatially varying scatter response function for scatter compensation in SPECT imaging," *IEEE Trans. Nucl. Sci.* **40**, 1192–1197 (1993).

<sup>19</sup>C. Kamphuis, F. J. Beekman, P. P. van Rijk, and M. A. Viergever, "Dual matrix ordered subsets reconstruction for accelerated 3D scatter compensation in single-photon emission tomography," *Eur. J. Nucl. Med.* **25**, 8–18 (1998).

<sup>20</sup>G. L. Zeng and G. T. Gullberg, "Unmatched projector/backprojector pairs in an iterative reconstruction algorithm," *IEEE Trans. Med. Imaging* **19**, 548–555 (2000).

<sup>21</sup>M.-A. Park, A. Mahmood, R. E. Zimmerman, N. Limpa-Amara, G. M. Makrigiorgos, and S. C. Moore, "Adsorption of metallic radionuclides on plastic phantom walls," *Med. Phys.* **35**, 1606–1610 (2008).

<sup>22</sup>B. E. Zimmerman, J. T. Cessna, and M. A. Millican, "Experimental determination of calibration settings for plastic syringes containing solutions of Y-90 using commercial radionuclide calibrators," *Appl. Radiat. Isot.* **60**, 511–517 (2004).

<sup>23</sup>Y. Du, B. M. W. Tsui, and E. C. Frey, "Partial volume effect compensation for quantitative brain SPECT imaging," *IEEE Trans. Med. Imaging* **24**, 969–976 (2005).

<sup>24</sup>N. Song, Y. Du, B. He, and E. C. Frey, "Development and evaluation of a model-based downscatter compensation method for quantitative I-131 SPECT," *Med. Phys.* **38**, 3193–3204 (2011).